P4.36 SURFACE EMISSIVITY DERIVED FOR INFRARED REMOTE SENSING FROM SATELLITES

Yan Chen, Sunny Sun-Mack
Science Applications International Corporation, Hampton, VA 23666

*Patrick Minnis, William L. Smith, Jr., David F. Young
Atmospheric Sciences, NASA Langley Research Center, Hampton, VA 23681

AMS 11th Conference on Satellite Meteorology and Oceanography
Madison, Wisconsin
October 15 – 18, 2001
pp. 512-515

P4.36 SURFACE EMISSIVITY DERIVED FOR INFRARED REMOTE SENSING FROM SATELLITES

Yan Chen, Sunny Sun-Mack
Science Applications International Corporation, Hampton, VA 23666

*Patrick Minnis, William L. Smith, Jr., David F. Young
Atmospheric Sciences, NASA Langley Research Center, Hampton, VA 23681

1. INTRODUCTION

Surface emissivity is essential for deriving the surface skin temperature from satellite-based infrared measurements and for estimating the emission of longwave radiation from the surface, an important component of the energy budget of the surface-atmosphere interface. It is also critical for cloud detection and retrieval of cloud properties. Brightness temperature differences *BTD* between 3.7 and 11-µm observations are often indicative of the presence or absence of clouds. For clear scenes, the *BTD* is due to differences in atmospheric absorption and in surface emissivity ε between the two channels. Cloud phase, optical depth, and particle size further affect the *BTD* in cloudy scenes. Retrieval of cloud phase and effective particle size often relies on the value of *BTD*, which for optically thin clouds is affected by the surface emission and, at 3.7 µm, the surface reflectance. Thus, the accuracy of cloud detection and particle size retrievals depends on the accuracy of the surface emissivity. The Clouds and Earth's Radiant Energy System (CERES, Wielicki et al. 1998) system is measuring broadband shortwave and longwave radiances and deriving cloud properties from various imagers to produce a combined global radiation and cloud property data set (Minnis et al. 1999). This paper presents the development and results of an analysis of satellite imager data taken at 3.7, 10.8, and 12.0 µm to derive a seasonally varying map of ε for use by CERES and other cloud retrieval algorithms.

2. DATA

ISCCP (International Satellite Cloud Climatology Project) DX Advanced Very High Resolution Radiometer (AVHRR) data taken during 1986 were used to obtain the clear-sky top-of-the-atmosphere (TOA) brightness temperatures T_i at 3.7, 10.8, and 12.0 µm, channels i = 3, 4, and 5, respectively. These data have a nominal resolution of 4 km but are sampled every 32 km. It is assumed that the ISCCP scene classification (Rossow and Schiffer 1999) is correct for all pixels and, therefore, the temperatures are uncontaminated by clouds. Six-hourly ECMWF (European Center Medium Range Weather Forecast) analyses provided at a resolution of 0.56° latitude and longitude were used to specify the vertical profiles of atmospheric temperature, humidity, and ozone. Linear interpolation was used to match the soundings to the satellite observation times. Standard atmospheric values were used for profiles of other absorbing gases such as NO_2 and CH_4.

Corresponding author address: P. Minnis, MS 420 NASA Langley Res. Ctr., Hampton, VA 23681;
email: p.minnis@larc.nasa.gov

3. METHODOLOGY

The basic approach solves a set of simultaneous equations to obtain surface emissivity. The method requires observations from both daytime and nighttime over the same area.

The relationship between the TOA and surface radiances can be crudely represented as

$$B_i(T_i) = \varepsilon_{ai} B_i(T_{ai}) + (1-\varepsilon_{ai}) B_i(T_{si}) \quad (1)$$

where B is the Planck function, ε_a and T_a are the atmospheric effective emissivity and effective temperature, respectively. The radiance for T_{si}, the apparent skin radiating temperature, is determined using the correlated *k*-distribution method (Kratz 1995) with the atmospheric profiles to remove the molecular absorption. The *k*-distribution technique is used to compute the downwelling and upwelling radiation at each ECMWF layer over the entire band pass of the channel using the appropriate filter function for the particular satellite imager channel. Considering the downwelling atmospheric radiance at the surface L_a, the radiation balance at surface is

$$B_i(T_{si}) = \varepsilon_i B_i(T_{skin}) + (1-\varepsilon_i) L_{ai} \quad (2)$$

in the absence of solar radiation, where T_{skin} is the skin temperature and T_{si} is the effective radiating temperature of the surface. For simplicity, it assumed that ε_i does not depend on the viewing zenith angle VZA. Skin temperature can be expressed at night as

$$T_{skin} = B_i^{-1}[\{B_i(T_{si}) - L_{ai}\}/\varepsilon_i + L_{ai}], \quad (3)$$

where B_i^{-1} is the inverse Planck function. If the skin temperature is known, the emissivity can be solved for the remaining channels, e.g.,

$$\varepsilon_3 = [B_3(T_{s3}) - L_{a3}] \,/\, [B_3(T_{skin}) - L_{a3}]. \quad (4)$$

At night, both T_{s3} and T_{s4} can be derived using (2) and the emissivity ratio,

$$\varepsilon_3' = \varepsilon_3 / \varepsilon_4 = [B_3(T_{s3}) - L_{a3}] / [B_3(T_{s4}) - L_{a3}], \quad (5)$$

can be computed. If it is assumed that this ratio is a constant for a given surface, then the value of ε_3 can be determined from data taken during the daytime. However, the ratio is variable depending on L_{a3}, which changes with precipitable water *PW*. To account for this variation, the data can be fitted to an equation of the form

$$\varepsilon_3' = \varepsilon_{3o}' + a\,PW + b\,PW^2, \quad (6)$$

where ε_{3o}' is the baseline emissivity ratio and is generally close to the value obtained from (5) if $L_{a3} = 0$. The coefficients for (6) can be computed from data taken during the night for several different times to obtain a reasonable dynamic range in *PW*. During the daytime, the apparent surface temperature for channel 3 is

$$B_3(T_{s3}) = \varepsilon_3[B_3(T_{skin})] + \alpha_3[\chi S_3' + L_{a3}], \quad (7)$$

where χ is the anisotropic correction factor, α_3 is the surface albedo, and S_3', the solar radiation reaching the surface, is computed from the Earth-sun distance and solar-zenith-angle corrected solar constant attenuated by atmospheric absorption using the *k*-distribution method. According to the Kirchoff's law,

$$\alpha_3 = (1 - \varepsilon_3). \quad (8)$$

Using (4), (5), and (8) to substitute for the emitted component and the albedo on the right hand side of (7) and rearranging gives

$$\varepsilon_3 = 1 - \{B_3(T_{s3}) - \varepsilon_3' [B_3(T_{s4})] - (1 - \varepsilon_3')\, L_{a3}\}/\chi S_3'. \quad (9)$$

In this manner, ε_3 is derived using (9). The absorption coefficients used for the thermal component are applied to the observed 3.7-µm radiance to obtain $B_3(T_{s3})$. Although the atmospheric attenuation of the upwelling solar and emitted 3.7-µm radiances is slightly different for each component, the differences should have a negligible impact on the result. Knowing ε_3 , T_{skin} can easily be solved from (7). Then, ε_4 and ε_5 are computed from (3).

This technique was tested theoretically using 3 different surface types with ε_3 ranging from 0.73 to 0.97 and ε_4 ranging 0.93 to 0.99 using 91 soundings to represent a large range of atmospheric conditions. The resulting values of ε_3 were within 1% of the original value for all of the cases with the largest errors occurring for the desert (0.73) case. RMS errors up to 3% were found for ε_4 with the greatest errors occurring for the desert case. The mean errors were all negligible. The theoretical calculations assumed an isotropic surface reflectance and no VZA dependence of ε.

The ISCCP data were analyzed by computing ε_3' for each clear nighttime pixel and averaging the results for every 1° latitude-longitude box for a given orbit. The corresponding value of *PW* was saved for each average. Because of insufficient sampling, however, a mean value of ε_3' was computed for each region and used instead of a fit to (6) to derive ε_3, ε_4, and ε_5 from the daytime data to obtain mean values and standard deviations for each region. The values of χ used in (9) were taken from the models used by Trepte et al. (1999). Those models are generally used for visible or broadband solar channels. Averages were also computed for each IGBP surface type (Table 1) and then used to fill in the results for regions with no data excepting deserts. During daytime, the value of T_3 was often not used because it saturated over desert areas due to high afternoon skin temperatures and highly reflective surfaces. Linear interpolation between the available months was used to obtain a more realistic estimate of emissivity for each desert region individually when no T_3 data were available. ISCCP DX data from January, April, June and October, 1986 were processed in this manner.

4. RESULTS

Figure 1 shows the distribution of ε_3 derived for January and June 1986. The gray scale starts at 0.700, but several desert areas have lower values. The heavily vegetated areas have values greater than 0.925 while intermediate values are found over less vegetated regions. The means for each of the IGBP types for the Northern Hemisphere are summarized in Table 2. The greatest seasonal variations occur in the lightly vegetated savannahs, grasslands, shrublands, and deserts. The most barren deserts like the Sahara do not show much seasonal variation. Some of the IGBP types, like tundra and deciduous needleleaf forests, are not well sampled and are not reliable. The ocean and snow categories are probably cloud contaminated and are not used for CERES.

Table 1. Surface type.

IGBP Type
1. evergreen needleleaf = conifer
2. evergreen broadleaf = conifer
3. deciduous needleleaf = deciduous
4. deciduous broadleaf = deciduous
5. mixed forests = 1/2 conifer + 1/2 deciduous
6. closed shrublands = mosaic
7. open shrubland = mosaic
8. woody savannas = grass
9. savannas = grass
10. grasslands = grass
11. permanent wetlands = 1/2 grass + 1/2 water
12. croplands = grass
13. urban = black body
14. mosaic = 1/2 grass + 1/2 mixed forest
15. snow/ice
16. barren/sparsely vegetated = desert
17. water
18. tundra = frost
19. coastline = 10% to 90% water

Table 2. Mean ε_3 for Northern Hemisphere.

IGBP	January	April	June	October
1	0.947	0.951	0.964	0.928
2	0.954	0.956	0.958	0.965
3	-------	0.929	0.963	0.941
4	0.942	0.943	0.957	0.953
5	0.953	0.945	0.964	0.946
6	0.908	0.933	0.944	0.924
7	0.827	0.873	0.932	0.861
8	0.919	0.930	0.951	0.947
9	0.874	0.926	0.924	0.933
10	0.864	0.899	0.924	0.901
11	0.928	0.951	0.956	0.901
12	0.913	0.924	0.939	0.923
13	0.917	0.929	0.944	0.937
14	0.915	0.926	0.942	0.927
15	0.924	0.972	0.969	0.954
16	0.772	0.866	0.921	0.797
17	0.951	0.973	0.973	0.962
18	0.935	0.968	0.949	0.929
19	0.929	0.952	0.959	0.939

The values for ε_4 and ε_5 were generally much greater than their ε_3 counterparts. In some cases the values exceed unity, indicating errors in the retrievals.

To assess the results, the TOA channel-3 brightness temperatures were calculated using the emissivity maps, the observed values of T_4, and the ECMWF profiles. Two data sets were used: January 1986 ISCCP DX and January 1998 Visible Infrared Scanner (VIRS) data used by CERES. Differences between the predicted and observed values of T_3 are summarized in Tables 3 and 4. Except for snow, tundra, savannah, and open shrubland, the mean daytime errors are 1K or less and the standard deviations range between 2 and 4K. The nighttime results are biased by 1 to 5 K; the largest values occur over deserts. A diurnal variation in ε_3 was found by Minnis et al. (1998) that is roughly equivalent to the day-night differences seen in Table 3. The VIRS results are similar to those for AVHRR over heavily forested areas, but over other surface types, the predicted temperatures are generally much greater by 1 to 5K with much larger standard deviations. These differences indicate that ε_3 for the VIRS 3.7-μm channel is considerably greater than the corresponding AVHRR-based value. The source of these large differences is not readily apparent.

Table 3. T_3 errors using ε_3 for January 1986 DX data.

	ΔT (K)			
IGBP	Daytime		Nighttime	
	mean	std	mean	std
1	0.5	2.3	1.7	1.7
2	-0.6	3.4	0.2	3.0
3	----	----	----	----
4	0.4	2.8	1.4	2.1
5	0.5	2.4	1.4	1.7
6	0.8	2.8	1.9	2.0
7	3.9	5.5	3.1	3.0
8	0.7	2.9	1.3	2.2
9	2.0	3.9	1.7	2.3
10	1.3	4.1	3.0	3.3
11	0.6	2.2	1.0	1.9
12	0.4	3.0	1.9	2.6
13	-0.6	3.0	2.0	3.0
14	0.6	3.1	1.7	2.7
15	1.7	6.3	2.1	9.8
16	0.4	2.9	5.5	3.0
17	0.8	3.1	1.0	1.7
18	2.1	4.5	4.7	4.2
19	-0.4	3.9	1.3	3.0

Table 4. T_3 errors using ε_3 for Jan. 1998 VIRS data.

	ΔT (K)			
IGBP	Daytime		Nighttime	
	mean	std	mean	std
1	0.9	3.6	0.9	3.0
2	0.2	4.0	0.4	2.7
3	----	----	----	----
4	-1.1	4.2	-0.5	4.2
5	0.5	4.0	-0.4	3.5
6	-3.8	5.6	-1.5	3.6
7	-2.5	7.1	-2.6	4.0
8	-2.5	4.7	-0.7	3.0
9	-4.5	4.6	-1.1	2.8
10	-2.7	7.3	-1.8	4.3
11	1.3	4.8	0.7	3.7
12	-3.1	5.2	-0.4	3.2
13	-5.8	6.3	-1.9	4.6
14	-1.2	4.3	-0.1	3.4
15	8.3	7.6	-3.5	5.7
16	-2.1	5.5	-3.0	3.1
17	-0.7	3.0	0.7	1.2
18	-3.6	8.1	-3.2	5.2
19	-0.6	6.0	-1.7	5.0

5. CONCLUDING REMARKS

The results of the method applied here yield very reasonable daytime predictions of T_3 for the AVHRR data that were used in the original determination of the emissivities. The resulting bias in the nighttime data and even greater biases in the VIRS temperatures highlight the paucity of information about surface emissivity and the bidirectional reflectance characteristics at solar infrared (3.5 - 4.0 μm) wavelengths. The observed errors can arise for many different reasons: errors in the atmospheric profiles, large uncertainties in the anisotropic correction factors, spectral variability in surface emissivity, VZA-dependencies, small time and space scale changes of emissivity due to changes in surface moisture (e.g., dew), and residual cloud or ground fog contamination of the clear scenes. These and other factors will be explored to improve the determinations of surface emissivity for remote sensing.

References

Kratz, D. P., 1995: The correlated *k*-distribution technique as applied to the AVHRR channels. *J. Quant. Spectrosc. Radiat. Transfer*, **53**, 501--517.

Minnis, P., W. L. Smith, Jr., and D. F. Young, 1998: Surface emissivity derived from multispectral satellite data. Proc. *8th Annual ARM Sci. Team Mtg.*, Tuscon, AZ, March 23-27, 1998, 489-494.

Minnis, P., D. F. Young, B. A. Wielicki, P. W. Heck, S. Sun-Mack, and T. D. Murray, 1999. Cloud properties derived from VIRS for CERES. *Proc. AMS 10th Conf. Atmos. Rad.*, Madison, WI, June 28 – July 2, 21-24.

Rossow, W. B. and R. A. Schiffer, 1999: Advances in understanding clouds from ISCCP. *Bull Am. Meteor. Soc.*, **80**, 2261-2287.

Trepte, Q., Y. Chen, S. Sun-Mack, P. Minnis, D. F. Young, B. A. Baum, and P. W. Heck, 1999: Scene identification for the CERES cloud analysis subsystem. *Proc. AMS 10th Conf. Atmos. Rad.*, Madison, WI, June 28 – July 2, 1999, 169-172.

Wielicki, B. A., et al., 1998, Clouds and the Earth's Radiant Energy System (CERES): Algorithm overview. *IEEE Trans. Geosci. Remote Sens.*, **36**, 1127-1141.

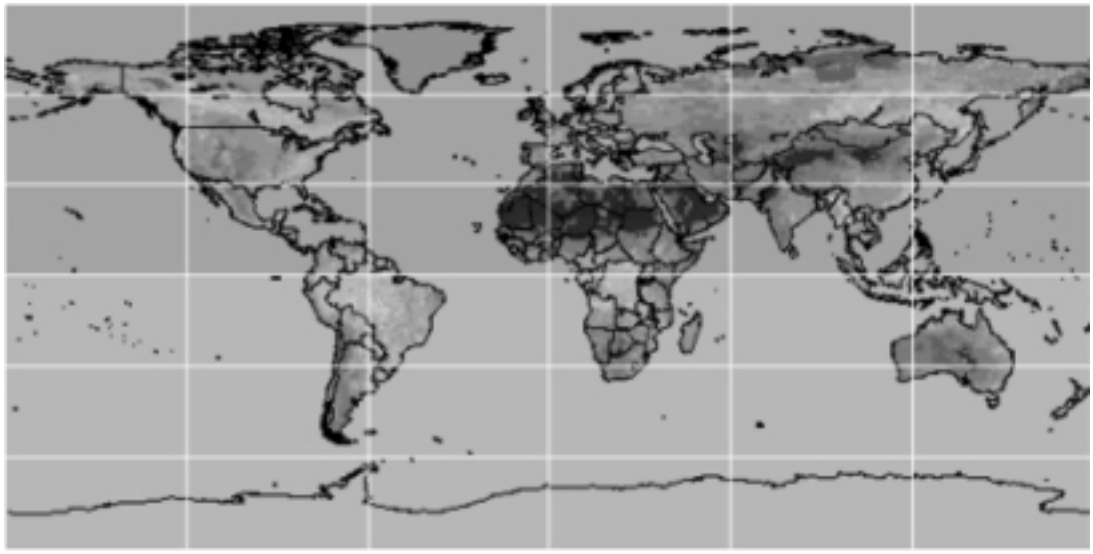

January 1986

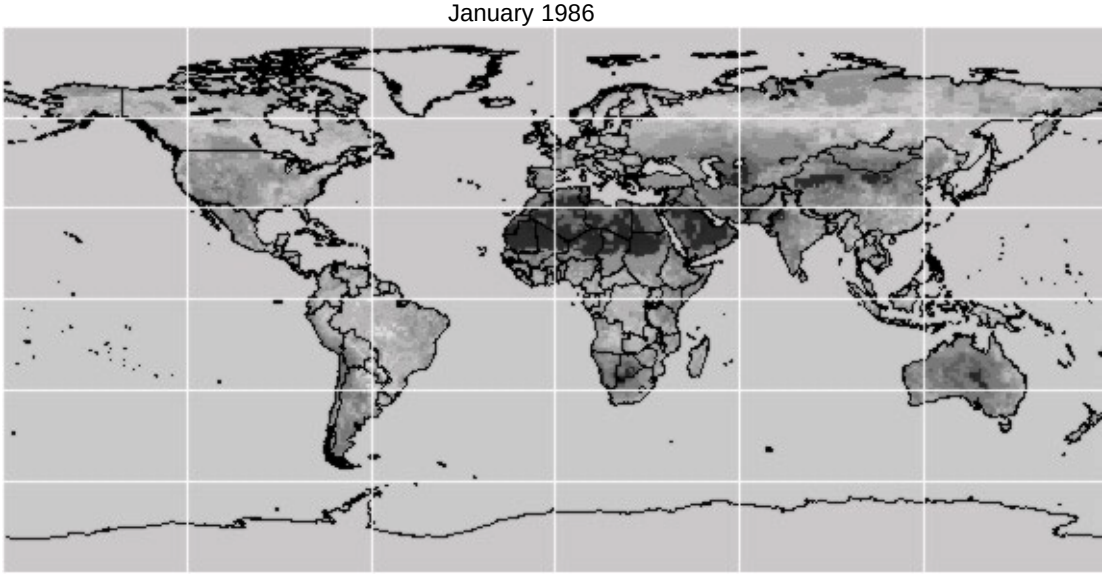

June 1986

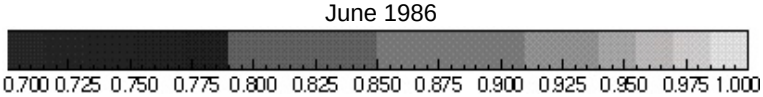

Fig. 1. Monthly mean 3.7-μm surface emissivities derived from AVHRR data during 1986.